ELSEVIER

Wave Motion 35 (2002) 205–221

WAVE MOTION

www.elsevier.com/locate/wavemoti

Paraxial geometrical optics for quasi-P waves: theories and numerical methods

Jianliang Qian [a], William W. Symes [b,*]

[a] *Institute for Mathematics and its Applications, University of Minnesota, 400 Lind Hall, 207 Church Street S.E., Minneapolis, MN 55455, USA*
[b] *The Rice Inversion Project, Department of Computational and Applied Mathematics, Rice University, Houston, TX 77251-1892, USA*

Received 1 December 2000; received in revised form 10 April 2001; accepted 25 May 2001

Abstract

The quasi-P wave in anisotropic solids is of practical importance in obtaining maximal imaging resolution in seismic exploration. The geometrical optics term in the asymptotic expansion for the wave characterizes the high frequency part of the quasi-P wave by using two functions: a phase (traveltime) function satisfying an eikonal equation and an amplitude function satisfying a transport equation. Based on a paraxial eikonal equation satisfied by the traveltime corresponding to the quasi-P downgoing waves, two new advection equations for take-off angles provide essential ingredients for computing amplitude functions on uniform Cartesian grids. However, the radiation problem of the eikonal equation has an upwind singularity at the point source which renders all finite-difference eikonal solvers to be first-order accurate near the source. Extending an isotropic adaptive eikonal solver to the paraxial quasi-P eikonal equations can treat this singularity efficiently and yield highly accurate traveltimes and amplitudes. Numerical experiments for quasi-P traveltimes and amplitudes in transversely isotropic media with vertical symmetry axes verify that the numerical methods are efficient and accurate. © 2002 Published by Elsevier Science B.V.

1. Introduction

In modern seismic exploration for hydrocarbon reservoirs, the quasi-P wave in anisotropic solids is of practical importance in both improving maximum imaging resolution and obtaining accurate estimates of elastic parameters [1,6,8,10,11,29,44,45], because shales among many others rocks are anisotropic at different length scales in the subsurface structure.

In practice, one takes surface reflection surveys and then inverts these surface reflection data by solving appropriate inverse problems. To solve these inverse problems, the industry favors the direct linearized method which seeks direct, closed form solutions by utilizing inverse scattering techniques such as the Born (or Rytov) approximation and the asymptotic ray theory [3,4,6,11,42], because the computation cost of the direct linearized method is cheaper than other methods such as nonlinear optimization technique. With the help of Fourier integral operator theory [43], the closed form solutions for the inverse problem are then obtained by analytical mappings, such as generalized radon transform (GRT), which require further asymptotic approximations [10,41].

* Corresponding author.
E-mail addresses: qian@ima.umn.edu (J. Qian), symes@caam.rice.edu (W.W. Symes).

0165-2125/02/$ – see front matter © 2002 Published by Elsevier Science B.V.
PII: S0165-2125(01)00102-0

The asymptotic theory originated in the field of geometrical optics [5], and the progressing wave expansion for the asymptotic method involves a "phase function" and an infinite sequence of "amplitude functions". The phase function satisfies a nonlinear partial differential equation of first-order called the eikonal equation; the amplitude functions satisfy a sequence of successive "transport equations" [9,20]. The leading term in the progressing wave expansion can be constructed in terms of quantities which occur in the geometrical optics; therefore, the leading term is called the *geometrical optics term* by Keller and Lewis [20]. The asymptotic method has been successfully used to construct the asymptotic solution for acoustic wave equations [20,41], deep-water wave equations [50], Maxwell's equations [5,20] and linear elastodynamic wave equations [2,6,7,11,16,17,25], among others.

For the linear elastodynamic wave equation in general elastic anisotropic solids, three different waves, i.e., quasi-longitudinal (*quasi-P*) and two quasi-transverse waves, are coupled together [16,25] for media of symmetries lower than those of transversely isotropic media. Because the quasi-P wave is of practical importance in obtaining maximal imaging resolution in seismic exploration as aforementioned, we develop theories and numerical methods for constructing the geometrical optics term (the leading term) in the asymptotic expansions for quasi-P waves in anisotropic solids, where the phase function is the so-called *traveltime*. To obtain the traveltime and amplitude function, we solve the quasi-P eikonal equation and a variant of the transport equation by finite-difference methods.

The eikonal equation can be solved by the method of characteristics which constructs the characteristic curves called "rays." The traveltime function and the amplitude function satisfy linear ordinary differential equations along the rays. The methods based on the characteristic equations are called "ray-tracing methods" [7,28,40], and they work for both *isotropic* and *anisotropic* solids. But ray-tracing methods have some drawbacks. The nonuniform distribution of traveltime data from ray-tracing methods gives rise to cumbersome, expensive and inaccurate interpolations for the application in seismic imaging. Wavefront construction methods have similar difficulties [24,49].

Finite-difference eikonal solvers compute the approximate first-arrival times directly on a prespecified grid, involve rather simple data structures, and are easy to code efficiently [15,22,34,36–39,46,47]. However, extension of these methods to anisotropic wave propagations is not entirely straightforward. Qin and Schuster [35] and Eaton [14] extended the expanding-wavefront scheme developed by Qin et al. [34] to the anisotropic medium, but their extensions work only for 2D cases and have first-order accuracy only. Kim [21] proposed a second-order expanding-box eikonal solver for transversely isotropic solids, but it is not clear how to extend the approach to general anisotropic solids.

The finite-difference eikonal solvers mentioned above depend on the fact that for isotropic media the ray velocity vector, i.e., the *group velocity*, has the same direction as the traveltime gradient, i.e., the *phase velocity*, so that we can use the traveltime gradient as a reliable indicator of energy flow in extrapolating the traveltime field. However, this is not true for anisotropic media [12]. Therefore, making use of the convexity of quasi-P slowness surface, Qian and Symes [33] established a reliable indicator of quasi-P ray velocity direction without computing the ray direction by formulating a relation between the group velocity direction and the phase velocity direction. The resultant eikonal equation is the so-called paraxial eikonal equation which has a built-in reliable indicator of the ray velocity direction. Furthermore, complete algorithm details and illustrative applications are presented in [31] for solving the heterogeneous quasi-P paraxial eikonal equation by using Newton methods and finite-difference methods (see also [30]).

Because the transport equation for the amplitude in the geometrical optics term involves second-order derivatives of the traveltime function, which in turn is obtained by numerical computations, it follows that to obtain first-order accurate amplitudes the computed traveltime function itself must have at least third-order accuracy. However, the eikonal equation with a point source has an upwind singularity at the source. To obtain highly accurate traveltime functions, we have to treat this singularity carefully. Zhang [51] and Vidale and Houston [48] reported the computation results for amplitudes in isotropic solids, but their computations were based on first-order eikonal solvers so that their results were inaccurate. Qian and Symes [32] proposed an adaptive gridding method to treat the upwind singularity, furthermore they used high-order finite-difference schemes for computing the traveltimes and amplitudes in isotropic solids; their results show that the adaptive gridding approach is efficient and highly accurate. Consequently, we extend this approach to compute the traveltimes and amplitudes in anisotropic solids.

In Section 2, we give some background on geometrical optics of quasi-P waves, including the eikonal equation for traveltimes and the transport equation for amplitudes. Section 3 presents the paraxial geometrical optics theories for quasi-P waves, including paraxial eikonal equations and two new advection equations for take-off angles needed in the computation of amplitudes. Section 4 introduces second- and third-order finite-difference schemes for paraxial eikonal equations, the schemes for solving the advection equations of take-off angles, and the adaptive gridding principle. To show the efficiency and accuracy of the adaptive gridding method, Section 5 presents some numerical examples for computing traveltimes, take-off angles and amplitudes in transversely isotropic solids with vertical symmetry axes (VTI). In the following presentation the Einstein summation convention is assumed [25].

2. Background on geometrical optics

Hooke's law states that stress σ_{ij} is related to strain e_{kl} by a stiffness tensor C_{ijkl}, $\sigma_{ij} = C_{ijkl}e_{kl}$. Therefore, by the symmetry of the stiffness tensor, the wave equation without body force is

$$\rho\frac{\partial^2 U_j}{\partial t^2} = \frac{\partial}{\partial x_i}\left(C_{ijkl}\frac{\partial U_k}{\partial x_l}\right), \tag{1}$$

where $\mathbf{U} = (U_i)$ is the displacement vector.

The progressing wave expansion [6,7,9] assumes that the solution is of the form

$$\mathbf{U}(\mathbf{x}, t) = \sum_{n=0}^{\infty}\mathbf{A}^{(n)}(\mathbf{x})\, f_n(t - \tau(\mathbf{x})), \qquad f'_{n+1} = f_n, \tag{2}$$

where the wavefront is

$$t = \tau(\mathbf{x}). \tag{3}$$

As can be seen, the individual terms in (2) become smoother as n increases, so the most singular part of the wave is captured by the leading terms $n = 0$ and $n = 1$. Substituting the *ansatz* (2) into the wave equation (1) and equating individual coefficients of f_{n-2} to zero successively, we have a recursive system for the phase τ and amplitudes $\mathbf{A}^{(n)}$. Because the *geometrical optics* term consisting of the phase and amplitude function is determined by the zeroth-order term ($n = 0$) and the first-order term ($n = 1$), we will mainly work with these two terms.

The zeroth-order term being zero gives rise to Christoffel's equation,

$$(\Gamma_{jk} - \delta_{jk})A_k^{(0)} = 0, \tag{4}$$

which leads to the eikonal equation for the phase function τ,

$$\det(a_{ijkl}p_i p_l - \delta_{jk}) = 0, \tag{5}$$

where $\mathbf{p} = (p_i) = \nabla\tau$ is the slowness vector normal to the wavefront (3); τ is the traveltime or phase of the wave mode; $a_{ijkl} = C_{ijkl}/\rho$ are the density-normalized elastic parameters; $\Gamma_{jk} = a_{ijkl}p_i p_l$; δ_{jk} is the Kronecker delta. Note that all of these quantities depend on the spatial coordinate vector $\mathbf{x} = (x_1, x_2, x_3)$, though in this and some of the following displays this dependence has been suppressed for the sake of clarity.

Next the first-order term being zero yields

$$(a_{ijkl}p_i p_l - \delta_{jk})A_k^{(1)} + p_i a_{ijkl}\frac{\partial A_k^{(0)}}{\partial x_l} + \rho^{-1}\frac{\partial}{\partial x_i}(\rho a_{ijkl}p_l A_k^{(0)}) = 0. \tag{6}$$

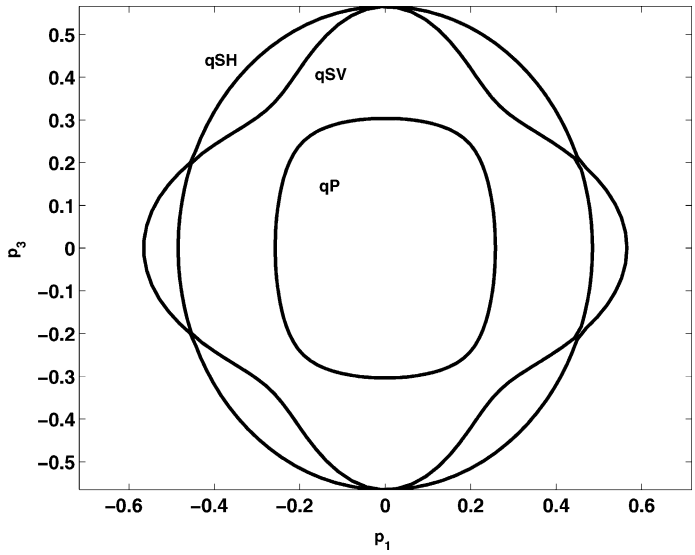

Fig. 1. The slowness surface for typical anisotropic media: a sextic surface which consists of three slowness sheets.

By the symmetry of the stiffness tensor a_{ijkl} and Eq. (4), Eq. (6) is reduced to a divergence form [6],

$$\frac{\partial(a_{ijkl}A_i^{(0)}A_k^{(0)}p_l)}{\partial x_j} = 0. \tag{7}$$

By Eq. (4), $\mathbf{A}^{(0)}$ is a multiple of the normalized eigenvector $\mathbf{g}$ of matrix (Γ_{jk}), hence the transport equation for the amplitude function is

$$\boldsymbol{\nabla} \cdot ((A^{(0)})^2\mathbf{v}) = 0,$$

where the group (ray) velocity vector $\mathbf{v} = (v_j)$ is used,

$$\frac{\mathrm{d}x_j}{\mathrm{d}t} = v_j = a_{ijkl}g_i g_k p_l. \tag{8}$$

Eq. (5) is a sextic polynomial equation in the slowness vector $\mathbf{p}$; that is, the slowness vector $\mathbf{p}$ lies on a sextic surface, which consists of three sheets, each surrounding the origin; see Fig. 1. By using $p_i = n_i/V$, where $\mathbf{n} = (n_i)$ is the unit normal vector to the wavefront and V is the normal or phase speed of the wavefront, Eq. (5) yields a cubic characteristic polynomial equation with respect to V^2, therefore it has three eigenvalues corresponding to a quasi-longitudinal ("quasi-P" or "qP") and two quasi-transverse waves. Moreover, experiment shows that the velocity of the quasi-P wave is always greater than those of the quasi-transverse waves ([16, p. 95]). Theoretically, Helbig and Schoenberg [18] showed that, for a transversely isotropic medium with the x_3 axis the transverse axis, when $a_{1133} + a_{3232} < 0$, there exists a direction of slowness vector $\mathbf{p}$ such that the first-arrival in that direction is a purely transverse wave; however, this kind of medium is unusual, "anomalous." Therefore, the present work will consider only the usual cases and assume that no anomalous polarization exists in the wave propagation [18]. Hence, the largest eigenvalue of the characteristic equation corresponding to the quasi-P wave propagation is simple (uniquely defined), and the quasi-P slowness sheet is the innermost one detached from the other two sheets. Furthermore, the quasi-P slowness sheet is *convex* ([25, p. 92]). The convexity of quasi-P slowness sheet is essential in constructing the paraxial approximation for the quasi-P eikonal equation.

3. Paraxial geometrical optics for quasi-P waves: theories

The Christoffel matrix $\Gamma_{jk} = a_{ijkl} p_i p_l$ is positive definite and scales as $p^2 = \mathbf{p} \cdot \mathbf{p}$. Therefore, each eigenvalue takes the form $v^2(\mathbf{x}, \mathbf{p}) p^2$, where v is a homogeneous function of degree zero in $\mathbf{p}$. Because the largest eigenvalue, denoted $v^2_{\mathrm{qP}}(\mathbf{x}, \mathbf{p})$, is simple, it depends smoothly on the components of the Christoffel matrix, i.e., on $\mathbf{p}$ and the stiffness tensor. The slowness vector $\mathbf{p}$ for which

$$S(\mathbf{x}, \mathbf{p}) \equiv |\mathbf{p}| v_{\mathrm{qP}}(\mathbf{x}, \mathbf{p}) = 1 \tag{9}$$

forms the *qP slowness surface*, and v_{qP} is the qP phase velocity. Note that these vectors solve the Christoffel equation (5).

The qP eikonal equation results from combining the slowness surface condition (9) with the slowness identity $\mathbf{p} = \nabla\tau$:

$$S(\mathbf{x}, \nabla\tau) = 1. \tag{10}$$

The method of characteristics relates its solution τ of the slowness surface equation (10) to the rays of geometrical optics, which are the solutions of the ordinary differential equations

$$\frac{\mathrm{d}\mathbf{x}}{\mathrm{d}t} = \nabla_{\mathbf{p}} S(\mathbf{x}, \mathbf{p}), \tag{11}$$

$$\frac{\mathrm{d}\mathbf{p}}{\mathrm{d}t} = -\nabla_{\mathbf{x}} S(\mathbf{x}, \mathbf{p}), \tag{12}$$

where the homogeneity of the eigenvalue v_{qP} in $\mathbf{p}$ is used, so that $\tau = t$ has the dimension of time.

Downgoing rays correspond to the part of the slowness surface on which $\mathrm{d}x_3/\mathrm{d}t > 0$. In [33], the convexity of quasi-P slowness surface is used to introduce a function H to pick out the part of a quasi-P slowness surface which corresponds to the downgoing rays; then the function H is modified to obtain a paraxial Hamiltonian H_Δ, which is defined in the whole horizontal slowness space. We summarize main results from [33] in the notation of this paper:

- for each $\mathbf{x}$ and horizontal slowness vector (p_1, p_2), there are at most two choices of p_3 for which $\mathbf{p} = (p_1, p_2, p_3)$ solves slowness surface equation (10) because of the convexity;

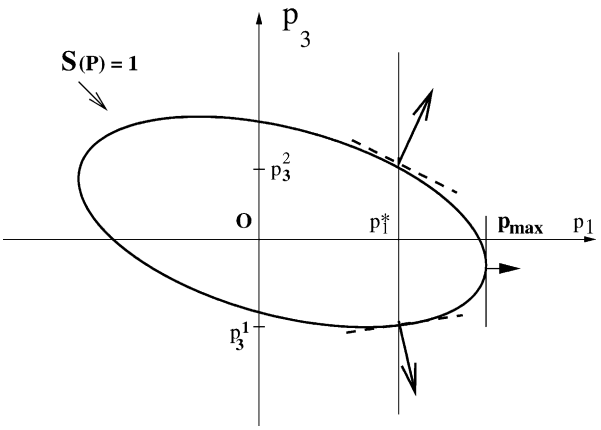

Fig. 2. The p_3 components of outward normals at the two intersections on the convex slowness surface have opposite signs.

- when two distinct solutions exist, only one satisfies (Fig. 2)

$$\frac{\mathrm{d}x_3}{\mathrm{d}t} = \frac{\partial S(\mathbf{x}, \mathbf{p})}{\partial p_3}(\mathbf{x}, \mathbf{p}) > 0,$$

  which corresponds to the downgoing rays;
- the above choice defines p_3 as a function of $\mathbf{x}$, p_1, p_2:

$$p_3 = H(\mathbf{x}, p_1, p_2), \tag{13}$$

  where H is a concave Hamiltonian;
- parametrize the horizontal variables (p_1, p_2) by polar coordinates: $(p_1, p_2) = (p' \cos\phi, p' \sin\phi)$ where $p' = \sqrt{p_1^2 + p_2^2}$. For each planar angle ϕ, the family of planes perpendicular to $(\cos\phi, \sin\phi, 0)$ is tangent to the slowness surface at exactly one point $(p'_{\max}(\phi)\cos\phi, p'_{\max}(\phi)\sin\phi, p_3(\phi))$ (see Fig. 2);
- choosing $0 < \Delta < 1$, define function H_Δ:

$$H_\Delta(p_1, p_2) = \begin{cases} H(p_1, p_2) & \text{if } p \le (1-\Delta)p'_{\max}(\phi), \\ H((1-\Delta)p'_{\max}(\phi)\cos\phi, (1-\Delta)p'_{\max}(\phi)\sin\phi), & \text{else,} \end{cases}$$

- the *paraxial eikonal equation* is

$$\frac{\partial \tau}{\partial x_3} = H_\Delta\left(\mathbf{x}, \frac{\partial \tau}{\partial x_1}, \frac{\partial \tau}{\partial x_2}\right). \tag{14}$$

Next we consider how to compute quasi-P wave amplitudes in Cartesian coordinates. If rays start from the point source, i.e. the so-called radiation problem, the amplitude $A \equiv A^{(0)}$ satisfies that [6,10]

$$A(\tau) = \frac{1}{4\pi(\rho(\mathbf{s})\rho(\mathbf{x}))^{1/2} M^{1/2}} \tag{15}$$

with

$$M = |v(\mathbf{s})| V(\mathbf{x}) \frac{\mathrm{d}W(\mathbf{x}, \mathbf{s})|_{\mathbf{x}}}{\mathrm{d}S(\mathbf{s})|_{\mathbf{s}}}. \tag{16}$$

Here $V(\mathbf{x})$ is the qP phase velocity at $\mathbf{x}$; $\mathrm{d}S(\mathbf{s})$ and $\mathrm{d}W(\mathbf{x}, \mathbf{s})$ are surface area elements of the slowness surface Ω at $\mathbf{s}$ and the wavefront W at $\mathbf{x}$, respectively; see [6] for explanation of this mapping.

To expedite the numerical implementation, we introduce the so-called ray coordinates τ, q_1, q_2, where q_1 and q_2 are the ray parameters of the ray. In the case of a point source, q_1 and q_2 can be taken as take-off angles of the ray at the source. q_1 and q_2 characterize the given ray, and τ characterizes the position of the point on the ray. τ, q_1 and q_2 can be considered to be the curvilinear coordinates on the wavefront; that is,

$$x_i = x_i(\tau, q_1, q_2).$$

Also, q_1 and q_2 parametrize the slowness surface $\Omega(\mathbf{s})$,

$$p_i = p_i(q_1, q_2), \quad i = 1, 2, 3,$$

for $\mathbf{p} = (p_1, p_2, p_3)$ on $\Omega(\mathbf{s})$.

By ray coordinates, the surface area elements on the wavefront and slowness surface are, respectively,

$$\mathrm{d}W(\mathbf{x}, \mathbf{s}) = \left|\frac{\partial \mathbf{x}}{\partial q_1} \times \frac{\partial \mathbf{x}}{\partial q_2}\right| \mathrm{d}q_1\, \mathrm{d}q_2$$

and

$$\mathrm{d}S = \left| \frac{\partial \mathbf{p}}{\partial q_1} \times \frac{\partial \mathbf{p}}{\partial q_2} \right| \mathrm{d}q_1 \, \mathrm{d}q_2.$$

So finally we have

$$M = |v(\mathbf{s})| V(\mathbf{x}) \frac{|(\partial \mathbf{x}/\partial q_1) \times (\partial \mathbf{x}/\partial q_2)|_{\mathbf{x}}}{|(\partial \mathbf{p}/\partial q_1) \times (\partial \mathbf{p}/\partial q_2)|_{\mathbf{s}}}. \tag{17}$$

Because we want to compute the amplitude by finite-difference methods in Cartesian coordinates rather than in ray coordinates, we have to reformulate the amplitude formula in Cartesian coordinates.

To do so, note that the Jacobian from ray coordinates (τ, q_1, q_2) to Cartesian coordinates satisfies that

$$\frac{\partial(\mathbf{x})}{\partial(\tau, q_1, q_2)} = \left| \frac{\partial \mathbf{x}}{\partial \tau} \cdot \left(\frac{\partial \mathbf{x}}{\partial q_1} \times \frac{\partial \mathbf{x}}{\partial q_2} \right) \right| = V(\mathbf{x}) \left| \frac{\partial \mathbf{x}}{\partial q_1} \times \frac{\partial \mathbf{x}}{\partial q_2} \right|, \tag{18}$$

then it follows that

$$\left| \frac{\partial \mathbf{x}}{\partial q_1} \times \frac{\partial \mathbf{x}}{\partial q_2} \right| = \frac{1}{V(\mathbf{x})} \left(\frac{\partial(\tau, q_1, q_2)}{\partial(\mathbf{x})} \right)^{-1} = \frac{1}{V(\mathbf{x})} \frac{1}{|\nabla \tau \cdot (\nabla q_1 \times \nabla q_2)|}, \tag{19}$$

where ∇ is the gradient operator with respect to $\mathbf{x}$. Therefore, by Eq. (15),

$$A(\mathbf{x}; \mathbf{s}) = R(q_1(\mathbf{x}; \mathbf{s}), q_2(\mathbf{x}; \mathbf{s}))(|\nabla \tau \cdot (\nabla q_1 \times \nabla q_2)|)^{1/2}, \tag{20}$$

where the anisotropic radiation pattern is

$$R(q_1(\mathbf{x}; \mathbf{s}), q_2(\mathbf{x}; \mathbf{s})) = \frac{1}{4\pi (\rho(\mathbf{s})\rho(\mathbf{x})|v(\mathbf{s})|)^{1/2}} \left(\left| \frac{\partial \mathbf{p}}{\partial q_1} \times \frac{\partial \mathbf{p}}{\partial q_2} \right|_{\mathbf{s}} \right)^{1/2}. \tag{21}$$

In the above formula, the traveltime τ comes from the finite-difference solution of the paraxial eikonal equation. Now we derive two new advection equations to compute ∇q_1 and ∇q_2. Because along a ray the two ray parameters are constant, the derivatives of q_1 and q_2 with respect to τ vanish,

$$\frac{\mathrm{d}q_\nu}{\mathrm{d}\tau} = \frac{\partial q_\nu}{\partial x_i} \frac{\partial x_i}{\partial \tau} = 0, \tag{22}$$

where $\nu = 1$ or 2.

Once the traveltime τ is known, $v_i = (\partial x_i/\partial \tau)$ $(i = 1, 2, 3)$ can be computed from the ray equations (8). Therefore, equations (22) are advection equations in Cartesian coordinates for the two ray parameters q_1 and q_2,

$$v_i \frac{\partial q_\nu}{\partial x_i} = 0.$$

Because the paraxial eikonal equation characterizes the traveltime along downgoing rays, v_3 always has a positive lower bound; therefore, we can have evolution equations in depth direction $x_3 = z$ for the two ray parameters,

$$\frac{\partial q_\nu}{\partial x_3} = -\frac{v_1}{v_3} \frac{\partial q_\nu}{\partial x_1} - \frac{v_2}{v_3} \frac{\partial q_\nu}{\partial x_2}. \tag{23}$$

To finish the amplitude computation we still need to compute $\partial \mathbf{p}/\partial q_1$ and $\partial \mathbf{p}/\partial q_2$. Because the quasi-P slowness surface is convex, the mapping from the slowness vector to the group velocity vector is one-to-one; therefore, $\mathbf{p}$ is uniquely determined from known q_1 and q_2. Because the mapping from the slowness vector to the ray direction is explicit, we can solve a nonlinear system to obtain $\mathbf{p}^0$ from known q_1^0 and q_2^0 at a point $\mathbf{x}$,

$$q_\nu(p_1, p_2, H_\Delta(\mathbf{x}, p_1, p_2)) = q_\nu^0, \tag{24}$$

for example, Newton method can solve this system effectively [13].

The group (ray) velocity direction coincides with the energy flux direction [25], which is essential in extrapolating the traveltime field by finite-difference schemes. In *isotropic* solids, the group velocity direction is the same as the wavefront normal which appears in the eikonal equation explicitly, so the energy flux direction can be easily determined in order to extrapolate the traveltime field. However, in *anisotropic* solids the situation is completely different. Consequently, we have to incorporate the information of the group velocity direction into the paraxial Hamiltonian by some strategy. Naturally, at the outset we imposed an explicit aperture limitation on the group velocity vector, and this limitation in turn implies an implicit restriction on the slowness vector. However, the mapping from the group velocity vector to the slowness vector is implicit and the only readily available information is the slowness vector, so the explicit limitation on the group velocity vector cannot give rise to an efficient algorithm for the paraxial Hamiltonian. Due to the strict convexity of the slowness surface, the explicit limitation on the slowness surface as done in [33] also implies an implicit one on the group velocity vector. Therefore, this way leads to an efficient algorithm, and the resultant Hamiltonian has a built-in reliable indicator of the group velocity direction.

4. Paraxial geometrical optics for quasi-P waves: numerical methods

4.1. Numerical algorithms for paraxial Hamiltonian

First of all, due to the complexity of wave propagations in anisotropic solids, in general it is difficult to find an explicit form of the paraxial Hamiltonian. Therefore we have devised some numerical algorithms for computing the paraxial Hamiltonian. Since the theoretical results proved in [33] are constructive, the design of the algorithms in [30,31] basically follows those constructions. As a by-product, an algorithm is also designed for initializing the traveltime in finite-difference schemes.

4.2. High-order finite-difference schemes

Because the amplitude involved in the geometrical optics term is related to the second-order derivatives of traveltimes, a first-order accurate amplitude field requires a third-order accurate traveltime field. It is necessary to construct high-order accurate finite-difference schemes.

To increase the order of convergence of finite-difference schemes, we employ higher-order weighted essentially nonoscillatory (WENO) refinements which are based on ENO schemes. ENO schemes were introduced by Osher and Sethian [26] and Osher and Shu [27] for solving Hamilton–Jacobi equations; their essential principles are high-order interpolation with adaptive stencils which tries to avoid high gradient regions whenever possible. WENO schemes were first proposed by Liu et al. [23] to overcome the drawbacks of ENO's. Jiang and Peng [19] made further improvements and extensions for Hamilton–Jacobi equations.

Given mesh sizes Δx_1, Δx_2 and Δx_3, denote $\tau^n_{m,k}$ as the numerical approximation to the viscosity solution $\tau(x_1^m, x_2^k, x_3^n)$ of Eq. (14) at the grid point (x_1^m, x_2^k, x_3^n). Define the backward $(-)$ and forward $(+)$ first-order difference quotient approximations to the left and right derivatives of $\tau(x_1, x_2, x_3)$ at the location (x_1^m, x_2^k, x_3^n) with respect to x_1 and x_2 as

$$D^{\pm}_{x_1}\tau^n_{m,k} = \pm\frac{\tau^n_{m\pm1,k} - \tau^n_{m,k}}{\Delta x_1}, \qquad D^{\pm}_{x_2}\tau^n_{m,k} = \pm\frac{\tau^n_{m,k\pm1} - \tau^n_{m,k}}{\Delta x_2}. \tag{25}$$

The WENO second-order schemes for $D^{\pm}_{x_1}\tau_{m,k}$ are [19]

$$D^{-\mathrm{W},2}_{x_1}\tau_{m,k} = \tfrac{1}{2}(D^{+}_{x_1}\tau_{m-1,k} + D^{+}_{x_1}\tau_{m,k}) - \tfrac{1}{2}w_{-}(D^{+}_{x_1}\tau_{m-2,k} - 2D^{+}_{x_1}\tau_{m-1,k} + D^{+}_{x_1}\tau_{m,k}),$$
$$D^{+\mathrm{W},2}_{x_1}\tau_{m,k} = \tfrac{1}{2}(D^{+}_{x_1}\tau_{m-1,k} + D^{+}_{x_1}\tau_{m,k}) - \tfrac{1}{2}w_{+}(D^{+}_{x_1}\tau_{m+1,k} - 2D^{+}_{x_1}\tau_{m,k} + D^{+}_{x_1}\tau_{m-1,k}),$$

where

$$w_- = \frac{1}{1+2r_-^2}, \qquad r_- = \frac{\delta_1 + (D_{x_1}^- D_{x_1}^- \tau_{m,k})^2}{\delta_1 + (D_{x_1}^- D_{x_1}^+ \tau_{m,k})^2}, \tag{26}$$

$$w_+ = \frac{1}{1+2r_+^2}, \qquad r_+ = \frac{\delta_1 + (D_{x_1}^+ D_{x_1}^+ \tau_{m,k})^2}{\delta_1 + (D_{x_1}^- D_{x_1}^+ \tau_{m,k})^2}. \tag{27}$$

The WENO third-order schemes for $D_{x_1}^{\pm}\tau_{m,k}$ are [19]

$$D_{x_1}^{\pm \mathrm{W},3}\tau_{m,k} = \tfrac{1}{12}(-D_{x_1}^+\tau_{m-2,k} + 7D_{x_1}^+\tau_{m-1,k} + 7D_{x_1}^+\tau_{m,k} - D_{x_1}^+\tau_{m+1,k}) \pm \Delta x_1 \Phi^{\mathrm{WENO}}(D_{x_1}^- D_{x_1}^+\tau_{m\pm2,k}, D_{x_1}^- D_{x_1}^+\tau_{m\pm1,k}, D_{x_1}^- D_{x_1}^+\tau_{m,k}, D_{x_1}^- D_{x_1}^+\tau_{m\mp1,k}),$$

where

$$\Phi^{\mathrm{WENO}}(a,b,c,d) = \tfrac{1}{3}w_1(a-2b+c) + \tfrac{1}{6}(w_2 - \tfrac{1}{2})(b-2c+d)$$

with weights defined as

$$w_1 = \frac{\alpha_3}{\alpha_1+\alpha_2+\alpha_3}, \qquad w_2 = \frac{\alpha_2}{\alpha_1+\alpha_2+\alpha_3}, \qquad \alpha_1 = \frac{1}{(\delta_1+\beta_1)^2}, \qquad \alpha_2 = \frac{1}{(\delta_1+\beta_2)^2},$$
$$\alpha_3 = \frac{1}{(\delta_1+\beta_3)^2}, \qquad \beta_1 = 13(b-c)^2 + 3(b+c)^2, \qquad \beta_2 = 13(c-d)^2 + 3(3c-d)^2,$$
$$\beta_3 = 13(a-b)^2 + 3(a-3b)^2. \tag{28}$$

In the denominators of Eqs. (26)–(28), the small positive number δ_1 is added to avoid dividing by zero. The WENO second- and third-order schemes for $D_{x_2}^{\pm}\tau_{m,k}$ are defined similarly.

To adapt numerical schemes for Hamilton–Jacobi equations to the solution of eikonal equations, we need a so-called flux function $\hat{H}_\Delta$ defined by [27]

$$\hat{H}_\Delta(u^+,u^-,v^+,v^-) = \mathrm{ext}_{u\in I(u^-,u^+)}\mathrm{ext}_{v\in I(v^-,v^+)}H_\Delta(u,v), \tag{29}$$

the function $\mathrm{ext}_{u\in I(a,b)} = \max_{a\le u\le b}$ if $a \le b$, $\mathrm{ext}_{u\in I(a,b)} = \min_{b\le u\le a}$ else; $I(a,b) = [\min(a,b), \max(a,b)]$.

The second- and third-order WENO Runge–Kutta steps are

$$\delta_2^1\tau = \Delta x_3^{\mathrm{cfl}}\hat{H}_\Delta(D_{x_1}^{+\mathrm{W},2}\tau, D_{x_1}^{-\mathrm{W},2}\tau, D_{x_2}^{+\mathrm{W},2}\tau, D_{x_2}^{-\mathrm{W},2}\tau), \quad \tau^{(2,1)} = \tau + \delta_2^1\tau,$$
$$\delta_2^2\tau = \tfrac{1}{2}(\delta_2^1\tau + \Delta x_3^{\mathrm{cfl}}\hat{H}_\Delta(D_{x_1}^{+\mathrm{W},2}\tau^{(2,1)}, D_{x_1}^{-\mathrm{W},2}\tau^{(2,1)}, D_{x_2}^{+\mathrm{W},2}\tau^{(2,1)}, D_{x_2}^{-\mathrm{W},2}\tau^{(2,1)})),$$

and

$$\delta_3^1\tau = \Delta x_3^{\mathrm{cfl}}\hat{H}_\Delta(D_{x_1}^{+\mathrm{W},3}\tau, D_{x_1}^{-\mathrm{W},3}\tau, D_{x_2}^{+\mathrm{W},3}\tau, D_{x_2}^{-\mathrm{W},3}\tau), \quad \tau^{(3,1)} = \tau + \delta_3^1\tau,$$
$$\delta_3^2\tau = \tfrac{1}{4}(\delta_3^1\tau + \Delta x_3^{\mathrm{cfl}}\hat{H}_\Delta(D_{x_1}^{+\mathrm{W},3}\tau^{(3,1)}, D_{x_1}^{-\mathrm{W},3}\tau^{(3,1)}, D_{x_2}^{+\mathrm{W},3}\tau^{(3,1)}, D_{x_2}^{-\mathrm{W},3}\tau^{(3,1)})), \quad \tau^{(3,2)} = \tau + \delta_3^2\tau,$$
$$\delta_3^3\tau = \tfrac{1}{3}(2\delta_3^2\tau + 2\Delta x_3^{\mathrm{cfl}}\hat{H}_\Delta(D_{x_1}^{+\mathrm{W},3}\tau^{(3,2)}, D_{x_1}^{-\mathrm{W},3}\tau^{(3,2)}, D_{x_2}^{+\mathrm{W},3}\tau^{(3,2)}, D_{x_2}^{-\mathrm{W},3}\tau^{(3,2)})).$$

The depth step $\Delta x_3^{\mathrm{cfl}}$ must satisfy the stability condition (Courant–Friedrichs–Lewy condition),

$$\Delta x_3^{\mathrm{cfl}}\left(\max_{p_1,p_2}\sqrt{\left(\frac{\partial H_\Delta}{\partial p_1}\right)^2 + \left(\frac{\partial H_\Delta}{\partial p_2}\right)^2}\right) \le \frac{\Delta x_1 \Delta x_2}{\sqrt{\Delta x_1^2 + \Delta x_2^2}}, \tag{30}$$

with the maximum taken over the relevant range of p_1 and p_2. Since H_Δ is concave [33], inequality (30) reduces to

$$\Delta x_3^{\mathrm{cfl}} \left(\max_{\{(p_1^{\mathrm{e}}, p_2^{\mathrm{e}}):0\le\phi\le 2\pi\}} \sqrt{\left(\frac{\partial H_\Delta}{\partial p_1}\right)^2 + \left(\frac{\partial H_\Delta}{\partial p_2}\right)^2} \right) \le \frac{\Delta x_1 \Delta x_2}{\sqrt{\Delta x_1^2 + \Delta x_2^2}},$$

where $(p_1^{\mathrm{e}}, p_2^{\mathrm{e}}) = ((1-\Delta)p_{\max}(\phi)\cos\phi, (1-\Delta)p_{\max}(\phi)\sin\phi)$.

The jth-order scheme is then

$$\tau^{n+1} = \tau^n + \delta_j^j \tau^n$$

for $n = 0, 1, 2, \ldots$.

In isotropic media and transversely isotropic media with VTI, the above flux can be significantly simplified; see [33]. For example, for VTI media, the upwind jth order WENO approximations for $\partial\tau/\partial x_1$ and $\partial\tau/\partial x_2$ are

$$\hat{D}_{x_1}^j \tau = \mathrm{modmax}(\max(D_{x_1}^{-W,j}\tau, 0), \min(D_{x_1}^{+W,j}\tau, 0)),$$
$$\hat{D}_{x_2}^j \tau = \mathrm{modmax}(\max(D_{x_2}^{-W,j}\tau, 0), \min(D_{x_2}^{+W,j}\tau, 0)),$$

where the modmax function returns the larger value in modulus.

Consequently, the second- and third-order WENO Runge–Kutta steps are

$$\delta_2^1\tau = \Delta x_3^{\mathrm{cfl}} H_\Delta(\hat{D}_{x_1}^2\tau, \hat{D}_{x_2}^2\tau), \qquad \delta_2^2\tau = \tfrac{1}{2}(\delta_2^1\tau + \Delta x_3^{\mathrm{cfl}} H_\Delta(\hat{D}_{x_1}^2(\tau+\delta_2^1\tau), \hat{D}_{x_2}^2(\tau+\delta_2^1\tau))), \tag{31}$$

and

$$\delta_3^1\tau = \Delta x_3^{\mathrm{cfl}} H_\Delta(\hat{D}_{x_1}^3\tau, \hat{D}_{x_2}^3\tau), \qquad \delta_3^2\tau = \tfrac{1}{4}(\delta_3^1\tau + \Delta x_3^{\mathrm{cfl}} H_\Delta(\hat{D}_{x_1}^3(\tau+\delta_3^1\tau), \hat{D}_{x_2}^3(\tau+\delta_3^1\tau))),$$
$$\delta_3^3\tau = \tfrac{1}{3}(2\delta_3^2\tau + 2\Delta x_3^{\mathrm{cfl}} H_\Delta(\hat{D}_{x_1}^3(\tau+\delta_3^2\tau), \hat{D}_{x_2}^3(\tau+\delta_3^2\tau))). \tag{32}$$

4.3. Numerical schemes for advection equations of take-off angles

Once the traveltime is known, the advection equations of take-off angles are first-order linear hyperbolic equations, so we can use high-order WENO schemes to discretize the take-off angle derivatives. See [30] for details.

4.4. Adaptive gridding for the singularity at the source

The traveltime field is mostly smooth, and the use of upwind differencing in the eikonal solvers confines the errors due to singularities which develop away from the source point. The source point itself is, however, also an upwind singularity. The truncation error of a pth order method is dominated by the product of $(p+1)$th derivatives of the traveltime field and the $(p+1)$th power of the step(s).

For treating the upwind singularity at the source, Kim and Cook [22] refine the computational grid several times near the source so that the reduced grid spacing compensates for the increased truncation error near the source, which is similar to the adaptive gridding approach [32] we advocated for the isotropic solids. Thus we extend the adaptive-gridding approach in [32] to the anisotropic case, and the fundamental principle is similar to the isotropic case.

5. Numerical experiments

5.1. Geometrical optics for 2D VTI solids

In the case of VTI, an explicit form of the paraxial Hamiltonian can be found [33]; consequently we use that paraxial Hamiltonian in our numerical experiments. To simplify notation, in this section we use x and z instead of x_1 and x_3 to denote coordinates.

To be suitable for using adaptive gridding, a smoothed version of equation for 2D VTI is utilized:

$$\frac{\partial\tau}{\partial z} = H_{\theta_{\max}}\left(\frac{\partial\tau}{\partial x}\right) = \sqrt{\operatorname{smmax}\left(\frac{2c}{-b+\sqrt{b^2-4dc}}, \frac{\cos^2(\theta_{\max})}{v_{\mathrm{qP}}^2(\theta_{\max})}\right)}, \tag{33}$$

where

$$d \equiv \alpha_0^2\beta_0^2, \qquad b \equiv 2\alpha_0^2\beta_0^2\left(1+\delta+(\epsilon-\delta)\frac{\alpha_0^2}{\beta_0^2}\right)\left(\frac{\partial\tau}{\partial x}\right)^2 - \alpha_0^2 - \beta_0^2,$$

$$c \equiv \left((1+2\epsilon)\alpha_0^2\left(\frac{\partial\tau}{\partial x}\right)^2 - 1\right)\left(\beta_0^2\left(\frac{\partial\tau}{\partial x}\right)^2 - 1\right).$$

Here α_0, β_0, ϵ and δ are Thomsen's parameters [44] which are some combinations of the elastic parameters; the function smmax is a smoothed max function with $a > 0$,

$$\operatorname{smmax}(x,a) = \begin{cases} \frac{1}{2}a & \text{if } x < 0, \\ \frac{1}{2}a + 2\frac{x^4}{a^3}\left(1 - \frac{4}{5}\frac{x}{a}\right) & \text{if } 0 \le x < \frac{a}{2}, \\ x + 2\frac{(x-a)^4}{a^3}\left(1 + \frac{4}{5}\frac{x-a}{a}\right) & \text{if } \frac{a}{2} \le x < a, \\ x & \text{if } x \ge a. \end{cases}$$

As shown above, a certain Jacobian from Cartesian coordinates to ray coordinates is needed in the amplitude computation. Here the ray coordinates are defined by

$$(\tau, q_1) = (\tau(x, z; x_s, z_s), q_1(x, z; x_s, z_s)),$$

where τ and q_1 are the traveltime and take-off angle of a ray from source point (x_s, z_s) to a general point (x, z) in the subsurface, respectively.

In 2D anisotropic media with line sources, the amplitude satisfies the formula

$$A(x,z) = \frac{R(q_1(x,z;x_s,z_s))}{\sqrt{|J|}} = R(q_1(x,z;x_s,z_s))\sqrt{|\nabla\tau \times \nabla q_1|}. \tag{34}$$

In Eq. (34), R is the radiation pattern of the source and $J(x, z; x_s, z_s)$ is the Jacobian of the transformation from Cartesian coordinates (x, z) to ray coordinates (τ, q_1); ∇q_1 and $\nabla\tau$ are the gradients of the take-off angle and the traveltime, respectively.

The take-off angle q_1 satisfies an advection equation, which written in evolution form in depth is

$$\frac{\partial q_1}{\partial z} = -\frac{v_1}{v_3}\frac{\partial q_1}{\partial x}, \tag{35}$$

where for 2D VTI

$$v_1 = \frac{p_1(2\alpha_0^2(1+2\epsilon)\beta_0^2 p_1^2 + Bp_3^2 - \alpha_0^2(1+2\epsilon) - \beta_0^2)}{D}, \qquad v_3 = \frac{p_3(2\alpha_0^2\beta_0^2 p_3^2 + Bp_1^2 - \alpha_0^2 - \beta_0^2)}{D},$$

with

$$p_1 = \frac{\partial\tau}{\partial x}, \qquad p_3 = \frac{\partial\tau}{\partial z}, \qquad B = 2\alpha_0^2(\alpha_0^2(\epsilon-\delta) + \beta_0^2(1+\delta)),$$
$$D = 2 - (\alpha_0^2(1+\epsilon) + \beta_0^2)p_1^2 - (\alpha_0^2 + \beta_0^2)p_3^2.$$

As in the isotropic case, we use the adaptive-gridding approach for solving the paraxial eikonal equation (33). The technique for solving the advection equation of take-off angles in isotropic cases [32] could be modified to solve Eq. (35) as well, so the detail is omitted here.

5.2. Examples

To illustrate that the adaptive-gridding strategy is efficient and accurate for anisotropic media, we demonstrate some numerical experiments for a 2D VTI solid.

To compute the traveltime, the adaptive-gridding approach is used for solving the paraxial eikonal equation (33). To initialize the traveltime in homogeneous media, we use a bisection shooting method. The idea is, given the group angle, finding the corresponding slowness vector by a nonlinear iterative solver; then the group velocity gives the desired traveltimes. In addition, note that in the homogeneous anisotropic media the take-off angle and its derivatives have analytic forms, which we can use to calibrate the numerical results for the simple homogeneous media.

The example occupies the rectangle $\{-0.5\,\text{km} \le x \le 0.5\,\text{km}, 0 \le z \le 1\,\text{km}\}$; the source is located at $x_1 = 0.0\,\text{km}$, $x_3 = 0.0\,\text{km}$. The four Thomsen's parameters of homogeneous green river shale are $\alpha_0 = 3.330\,\text{km/s}$, $\beta_0 = 1.768\,\text{km/s}$, $\epsilon = 0.195$, $\delta = -0.220$. Since the parameter δ has the same magnitude as ϵ, the near-vertical anisotropic response is dominated by δ [44]; hence we use this example to demonstrate not only the accuracy of the adaptive-gridding approach but also the capability of the approach in capturing the anisotropy of wave propagation.

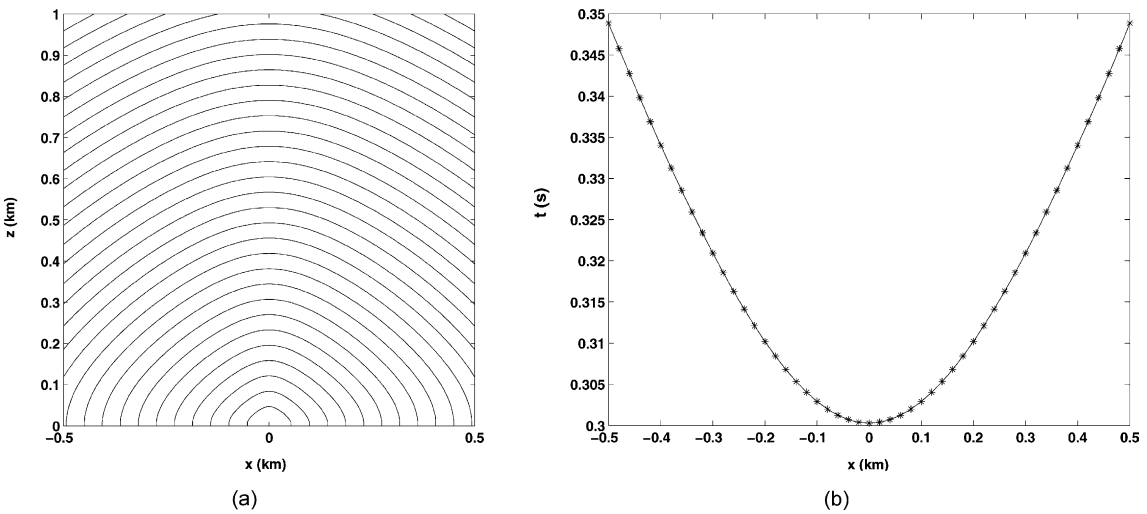

Fig. 3. (a) Traveltime contours for a 2D VTI model by the adaptive-gridding approach: anisotropic effects on the wave propagation are evident. (b) Traveltime comparison at $z = 1.0\,\text{km}$ for the model: adaptive-gridding traveltimes ($*$) and analytic traveltimes (–) match very well.

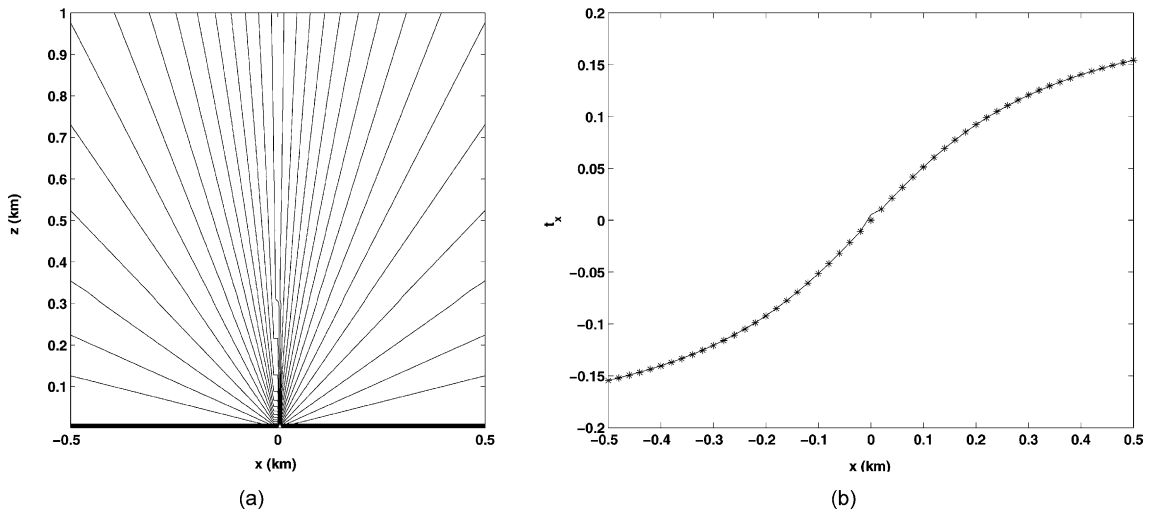

Fig. 4. (a) Contours of $\partial\tau/\partial x$ for a 2D VTI model by the adaptive-gridding approach. (b) Comparisons of $\partial\tau/\partial x$ at $z = 1.0$ km for the model: the adaptive-gridding solution ($*$) and analytic solution (–) match very well.

The grid sampling size is $\Delta x = \Delta z = 0.01$ km. The adaptive-gridding approach has a computational grid which is independent of the output grid. For the adaptive gridding, the maximum times of allowed grid refinement MAXREF is set to 5 with the coarsest grid 17×17, and the error tolerance is set to be 0.0001. To simplify the implementation for weak VTI media, we set the radiation pattern of the source to be constant (as stated above, we need to solve a nonlinear equation to get the anisotropic radiation pattern of the source, which will be addressed in a subsequent paper). The computational results are shown in Figs. 3–9.

Fig. 3(a) shows traveltime contours of the 2D VTI model, and the anisotropic effects on the wave propagation are evident. Fig. 3(b) shows the traveltime calibration at the bottom $z = 1$ km for the adaptive-gridding approach

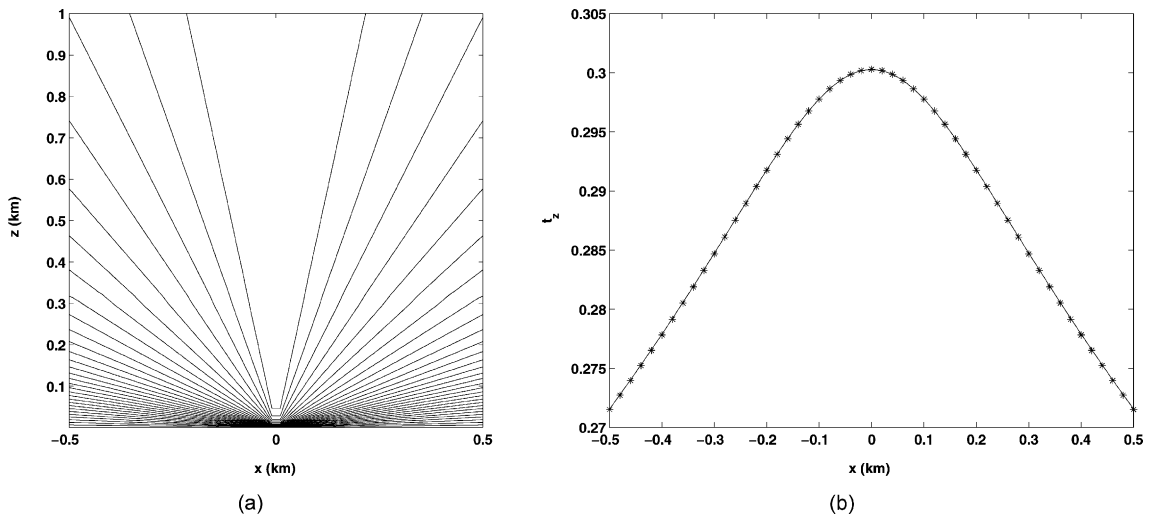

Fig. 5. (a) Contours of $\partial\tau/\partial z$ for a 2D VTI model by the adaptive-gridding approach. (b) Comparisons of $\partial\tau/\partial z$ at $z = 1.0$ km for the model: the adaptive-gridding solution ($*$) and analytic solution (–) match very well.

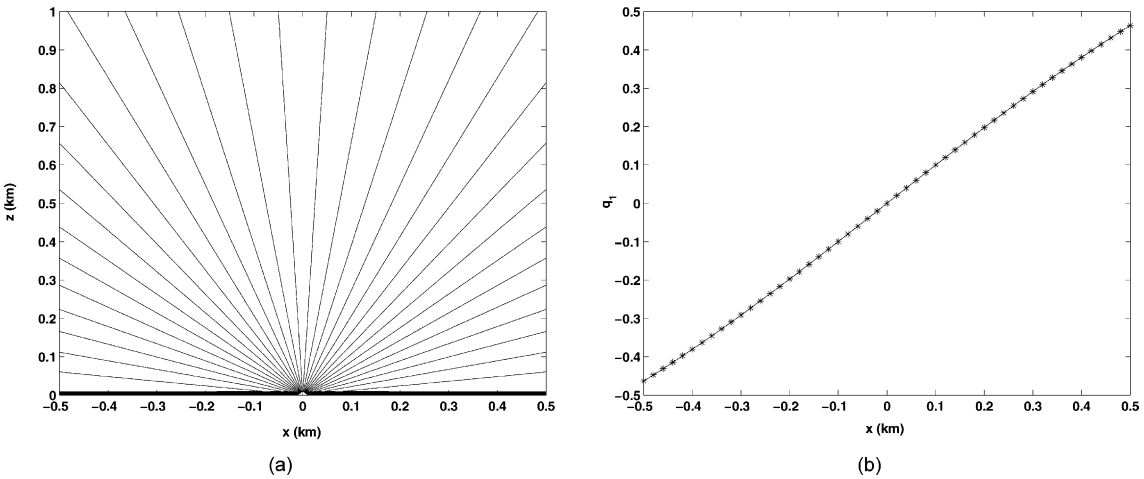

Fig. 6. (a) Take-off angles for a 2D VTI model by the adaptive-gridding approach: the contours are straight along the ray. (b) Take-off angle calibration at $z = 1.0$ km for the model: the adaptive-gridding solution ($*$) and analytic solution (–) match very well.

by using a bisection shooting method mentioned above; the comparison shows that the traveltimes by different approaches match very well.

Fig. 4(a) shows the contours of derivatives $\partial\tau/\partial x$ computed by the adaptive-gridding approach. Fig. 4(b) shows the calibration result for $\partial\tau/\partial x$. The analytical solution is computed by once again a shooting method, and the two computed derivatives match very well. Similar observations hold for derivatives $\partial\tau/\partial z$; see Fig. 5.

Now we will discuss the computational results for the take-off angle and its derivatives. Fig. 6(a) shows the contours for the take-off angles by the adaptive-gridding approach; the contours are straight lines because the rays in homogeneous anisotropic media are still straight. The analytical solution for take-off angles has an explicit form

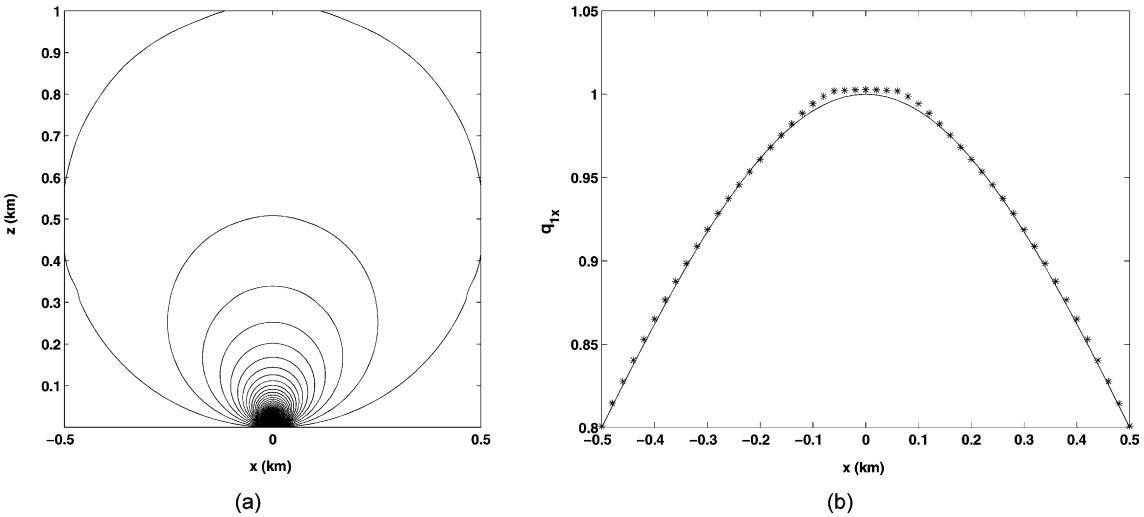

Fig. 7. (a) Contours of $\partial q_1/\partial x$ for a 2D VTI model by the adaptive-gridding approach. (b) Calibrations of $\partial q_1/\partial x$ at $z = 1.0$ km for the model. Since $q_1 = 0$ is a stationary point where the accuracy of numerical derivatives $\partial q_1/\partial x$ is poor, this inaccuracy is observed near the apex. Away from the stationary point, the adaptive-gridding solution ($*$) and analytic solution (–) match very well.

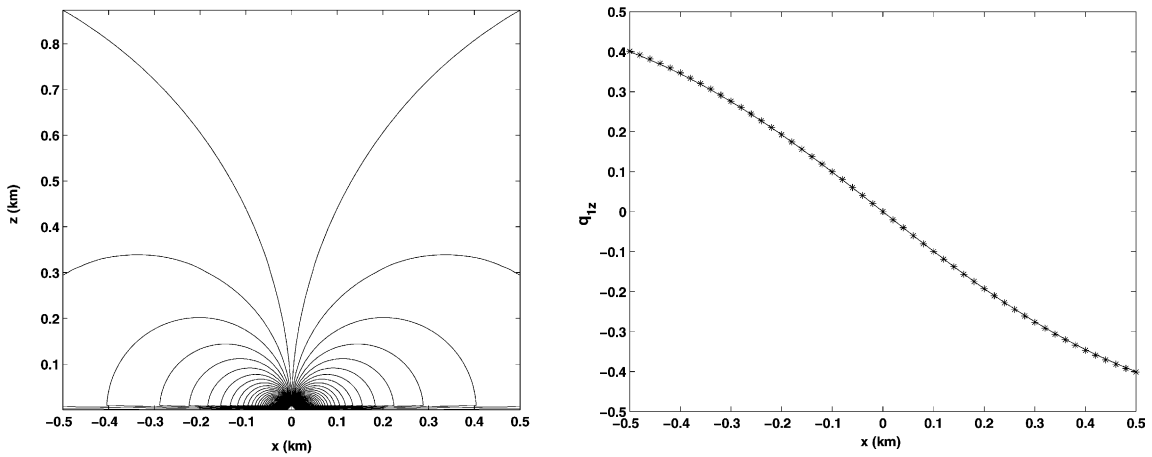

Fig. 8. (a) Contours of $\partial q_1/\partial z$ for a 2D VTI model by the adaptive-gridding approach. (b) Calibrations of $\partial q_1/\partial z$ at $z = 1.0$ km for the model: the adaptive-gridding solution ($*$) and analytic solution match very well.

now, therefore the calibration in Fig. 6(b) shows that the take-off angle computed by the adaptive-gridding approach is accurate.

Fig. 7(a) shows the contours of derivatives $\partial q_1/\partial x$ computed by the adaptive-gridding approach. Fig. 7(b) shows the calibration result at the bottom $z = 1$ km for the adaptive-gridding approach by using the analytical solution. Because $q_1 = 0$ is a stationary point where $\partial q_1/\partial x = 0$, the accuracy of numerical derivatives $\partial q_1/\partial x$ is poor;

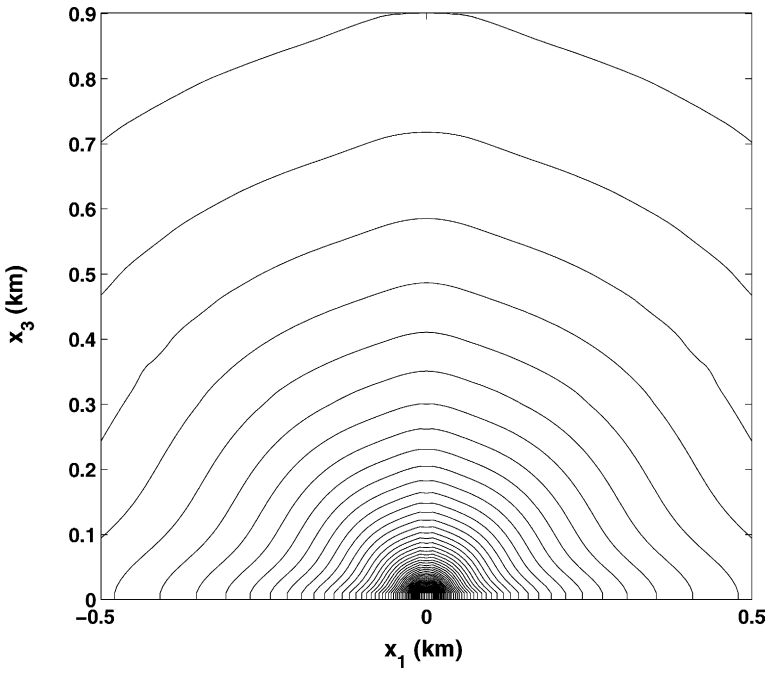

Fig. 9. Amplitude contours for a 2D VTI model by the adaptive-gridding WENO approach.

this inaccuracy is observed near the apex in Fig. 7(b). Away from the stationary point, the adaptive-gridding solution and analytic solution match very well. Fig. 8(a) shows the contours of derivatives $\partial q_1/\partial z$ computed by the adaptive-gridding approach. Fig. 8(b) shows the calibration result at the bottom $z = 1$ km for the adaptive-gridding approach by using the analytical solution, and the result demonstrates that the numerical derivatives $\partial q_1/\partial z$ are accurate.

Finally, Fig. 9 shows the amplitude field computed by the adaptive-gridding WENO approach. The amplitude field is smooth as expected.

The computational results have shown that the adaptive-gridding approach works very well for the traveltime and amplitude computation of the VTI solid. We expect that the approach can handle the traveltime and amplitude computation of the general anisotropic media as well.

6. Conclusions

The paraxial geometrical optics provides a framework for the computation of traveltimes and amplitudes of quasi-P waves by finite-difference methods on Cartesian grids. These quantities in turn could be used in Kirchhoff migration and inversion efficiently. To solve the paraxial eikonal equations to high-order accuracy, we introduced the second- and third-order WENO Runge–Kutta schemes. To treat the upwind singularity at the point source, we extend the adaptive gridding approach originally designed for isotropic solids to anisotropic solids. The numerical experiments for 2D VTI solids show that the algorithms are efficient and accurate. The implementation of the 3D version of the algorithms will be addressed elsewhere.

Acknowledgements

This work was partially supported by the National Science Foundation under grant number DMS 9627355, the Office of Naval Research under grant number N00014-96-1-0156, the US Department of Energy under grant number DE-FG07-97 ER14827 and the Rice Inversion Project. The authors thank Associate Editor Dr. C.H. Chapman and two anonymous reviewers for their constructive comments.

References

[1] J.E. Anderson, Imaging in transversely isotropic media with a vertical symmetry axis, Ph.D. Thesis, Center for Wave Phenomena, Colorado School of Mines, Golden, CO, 1996.
[2] J.G. Berryman, Long-wave elastic anisotropy in transversely isotropic media, Geophysics 44 (1979) 896–917.
[3] G. Beylkin, Imaging of discontinuities in the inverse scattering problem by inversion of a causal generalized radon transform, J. Math. Phys. 26 (1985) 99–108.
[4] G. Beylkin, R. Burridge, Linearized inverse scattering problem of acoustics and elasticity, Wave Motion 12 (1990) 15–22.
[5] M. Born, E. Wolf, Principles of Optics, Macmillan, New York, 1964.
[6] R. Burridge, M.V. de Hoop, D. Miller, C. Spencer, Multiparameter inversion in anisotropic media, Geophys. J. Int. 134 (1998) 757–777.
[7] V. Cerveny, Seismic rays and ray intensities in inhomogeneous anisotropic media, Geophys. J. Roy. Astr. Soc. 29 (1972) 1–13.
[8] A. Cherrett, S. Singh, Traveltime and polarization tomography in 3-D anisotropic media, in: Proceedings of the 68th Ann. Internat. Mtg., Soc. Expl. Geophys., Expanded Abstracts. Soc. Expl. Geophys. (1998) 1859–1862.
[9] R. Courant, D. Hilbert, Methods of Mathematical Physics, Vol. II, Wiley, New York, 1962.
[10] M.V. de Hoop, N. Bleistein, Generalized radon transform inversions for reflectivity in anisotropic elastic media, Inverse Probl. 13 (1997) 669–690.
[11] M.V. de Hoop, C. Spencer, R. Burridge, The resolving power of seismic amplitude data: an anisotropic inversion/migration approach, Geophysics 64 (1999) 852–873.
[12] J. Dellinger, W.W. Symes, Anisotropic finite-difference traveltimes using a Hamilton–Jacobi solver, in: Proceedings of the 67th Ann. Internat. Mtg., Soc. Expl. Geophys., Expanded Abstracts. Soc. Expl. Geophys. (1997) 1786–1789.

[13] J.E. Dennis Jr., R.B. Schnabel, Numerical Methods for Unconstrained Optimization and Nonlinear Equations, Prentice-Hall, Englewood Cliffs, NJ, 1983.
[14] D. Eaton, Finite difference traveltime calculation for anisotropic media, Geophys. J. Int. 114 (1993) 273–280.
[15] M.A. El-Mageed, 3D first arrival traveltimes and amplitudes via Eikonal and transport finite differences solvers, Ph.D. Thesis, Rice University, Houston, TX, 1996.
[16] F.I. Fedorov, Theory of Elastic Waves in Crystals, Plenum Press, New York, 1968.
[17] A.A. Fuki, Y.A. Kravtsov, O.N. Naida, Geometrical Optics of Weakly Anisotropic Media, Gordon and Breach, London, 1998.
[18] K. Helbig, M. Schoenberg, Anomalous polarization of elastic waves in transversely isotropic media, J. Acous. Soc. Am. 81 (1987) 1235–1245.
[19] G.S. Jiang, D. Peng, Weighted ENO schemes for Hamilton–Jacobi equations, SIAM J. Sci. Comput. 21 (2000) 2126–2143.
[20] J.B. Keller, R.M. Lewis, Asymptotic methods for partial differential equations: the reduced wave equation and Maxwell's equations, Surv. Appl. Math. 1 (1995) 1–82.
[21] S. Kim, Wavefronts of linear elastic waves: local convexity and modeling, Wave Motion 32 (2000) 203–216.
[22] S. Kim, R. Cook, 3-D traveltime computation using second-order ENO scheme, Geophysics 64 (1999) 1867–1876.
[23] X.D. Liu, S.J. Osher, T. Chan, Weighted essentially nonoscillatory schemes, J. Comput. Phys. 115 (1994) 200–212.
[24] Z. Meng, N. Bleistein, Wavefront construction ray tracing in tetrahedral models, CWP-251, Center for Wave Phenomena, Colorado School of Mines, Golden, CO, 1997.
[25] M.J.P. Musgrave, Crystal Acoustics, Holden-Day, San Francisco, CA, 1970.
[26] S.J. Osher, J.A. Sethian, Fronts propagating with curvature dependent speed: algorithms based on Hamilton–Jacobi formulations, J. Comput. Phys. 79 (1988) 12–49.
[27] S.J. Osher, C.W. Shu, High-order essentially non-oscillatory schemes for Hamilton–Jacobi equations, SIAM J. Num. Anal. 28 (1991) 907–922.
[28] V. Pereyra, Two-point ray tracing in general 3-D media, Geophys. Prosp. 40 (1992) 267–287.
[29] R. Pratt, C. Chapman, Traveltime tomography in anisotropic media-II: application, Geophys. J. Int. 109 (1992) 20–37.
[30] J. Qian, Geometrical optics for quasi-P waves: theories and numerical methods, Ph.D. Thesis, Rice University, Houston, TX, UMI Microform No. 9969308, 2000.
[31] J. Qian, W.W. Symes, Paraxial eikonal solvers for anisotropic quasi-P traveltimes, The Rice Inversion Project, Rice University, 2000 (http://www.trip.caam.rice.edu/).
[32] J. Qian, W.W. Symes, Adaptive finite difference method for traveltime and amplitude, Geophysics (2001), in press.
[33] J. Qian,W.W. Symes, Finite-difference quasi-P traveltimes for anisotropic media, Geophysics (2001), in press.
[34] F. Qin, Y. Luo, K.B. Olsen, W. Cai, G.T. Schuster, Finite difference solution of the eikonal equation along expanding wavefronts, Geophysics 57 (1992) 478–487.
[35] F. Qin, G.T. Schuster, First-arrival traveltime calculation for anisotropic media, Geophysics 58 (1992) 1349–1358.
[36] M. Reshef, D. Kosloff, Migration of common shot gathers, Geophysics 51 (1986) 324–331.
[37] W.A. Schneider Jr., Robust and efficient upwind finite-difference traveltime calculations in three dimensions, Geophysics 60 (1995) 1108–1117.
[38] W.A. Schneider Jr., K. Ranzinger, A. Balch, C. Kruse, A dynamic programming approach to first arrival traveltime computation in media with arbitrarily distributed velocities, Geophysics 57 (1992) 39–50.
[39] J.A. Sethian, A.M. Popovici, 3-D traveltime computation using the fast marching method, Geophysics 64 (1999) 516–523.
[40] P.M. Shearer, C.H. Chapman, Ray tracing in anisotropic media with a linear gradient, Geophys. J. 94 (1988) 575–580.
[41] W.W. Symes, Mathematics of reflection seismology, Annual Report, The Rice Inversion Project, Rice University, 1995. http://www.trip.caam.rice.edu/.
[42] W.W. Symes, R. Versteeg, A. Sei, Q.H. Tran, Kirchhoff simulation, migration and inversion using finite difference traveltimes and amplitudes, Annual Report, The Rice Inversion Project, Rice University, 1994. http://www.trip.caam.rice.edu/.
[43] M.E. Taylor, Partial Differential Equations: Basic Theory, Springer, Berlin, 1996.
[44] L. Thomsen, Weak elastic anisotropy, Geophysics 51 (1986) 1954–1966.
[45] I. Tsvankin, L. Thomsen, Inversion of reflection traveltimes for transverse isotropy, Geophysics 60 (1995) 1095–1107.
[46] J. van Trier, W.W. Symes, Upwind finite-difference calculation of traveltimes, Geophysics 56 (1991) 812–821.
[47] J. Vidale, Finite-difference calculation of travel times, Bull. Seis. Soc. Am. 78 (1988) 2062–2076.
[48] J.E. Vidale, H. Houston, Rapid calculation of seismic amplitudes, Geophysics 55 (1990) 1504–1507.
[49] V. Vinje, E. Iversen, H. Gjystdal, Traveltime and amplitude estimation using wavefront construction, Geophysics 58 (1993) 1157–1166.
[50] B.S. White, Wave action on currents with vorticity, J. Fluid Mech. 386 (1999) 329–344.
[51] L. Zhang, Imaging by the wavefront propagation method, Ph.D. Thesis, Stanford University, Stanford, CA, 1993.